Supplementary Information

Zincophilic Ion-Conductive Layer with Desolvation Effect and Oriented Deposition Behavior Achieving Superior Reversibility of Zn Metal Anode

Leilei Sun[a,b], Yang Wang[a,b,*], Guosheng Duan[a,b], Bin Luo[a,b], Sinan Zheng[a,b], Jingyun Huang[a,b,*], Zhizhen Ye[a,b,c,*]

[a] *State Key Laboratory of Silicon and Advanced Semiconductor Materials, School of Materials Science and Engineering, Zhejiang University, Hangzhou 310027, Zhejiang, China*
[b] *Zhejiang Provincial Engineering Research Center of Oxide Semiconductors for Environmental and Optoelectronic Applications, Institute of Wenzhou, Zhejiang University, Wenzhou 325006, China*
[c] *Shanxi-Zheda Institute of Advanced Materials and Chemical Engineering, Taiyuan 030032, Shanxi, China*

[*] Corresponding authors.

E-mail addresses: wangy_zju@zju.edu.cn (Y. Wang), huangjy@zju.edu.cn (J. Huang), yezz@zju.edu.cn (Zh. Ye)

Methods

Preparation of the ZnTe@Zn anode

The ZnTe@Zn anode is prepared by the method of thermal evaporation. The thermal evaporation coating machine (GSL-1800X-ZF4) is provided by Shenyang Kejing. Use the 10 × 10 cm^{-2} Zn foil (thickness: 100 μm) as the substrate and ZnTe with different weights (0.10-0.60 g; diameter range: 1-6 mm) as the target material. Vacuum to 10^{-5} Pa, then use the base rotation mode and adjust the evaporation current to 65-80 A to provide the temperature for ZnTe evaporation. After ZnTe finishes evaporating (about 15 min), the ZnTe@Zn anode is obtained. The optimization is carried out by electrochemical tests and further characterized by using XRD and SEM for the correspondence.

Electrochemical measurements

The Zn||Zn symmetric cell, Zn||Cu asymmetric cell, and Zn||α-MnO_2 full cell are assembled in CR2016 coin cell configurations. The electrolyte is conventional 2 M $ZnSO_4$ (an additional 0.1 M $MnSO_4$ in the full cell), and the separator used is glass fiber (Whatman, GF/A). LSV is conducted at a scan rate of 1 mV s^{-1} using Zn||Cu asymmetric cell with the electrolyte of 1 M Na_2SO_4. The Tafel curve is obtained by a three-electrode configuration, where bare Zn and ZnTe@Zn anodes are the working electrodes, the calomel electrode is the reference, and the Pt plate is the counter. EIS spectra are recorded with a frequency range from 0.1 Hz to 10^5 Hz with an AC voltage of 5 mV. CV measurement of the full cell and Zn||Cu cell is carried out at scan rates of 0.1 mV s^{-1} and 1 mV s^{-1}, respectively. The CA test is performed at a bias voltage of 150 mV.

DFT calculation:

To investigate the interaction at the ZnTe-electrolyte interface and the transport of Zn^{2+} in ZnTe, the density functional theory (DFT) calculations are performed with Vienna Ab-initio Simulation Package (VASP).[1-3] The exchange-correlation function is described by the Perdew-Burke-Ernzerh (PBE) in generalized gradient approximation (GGA),[4, 5] and the electron-ion interactions are implemented by the projector augmented-wave (PAW) method with an energy cutoff of 400 eV based on the plane wave method.[6, 7] The DFT-D3 method with Becke-Jonson damping dispersion correction is applied to take into account the van der Waals interaction. The implicit solvation model provided by the VASPsol code is used to consider the interactions between the aqueous solution (ε = 78.4 F·m^{-1}) and $Zn(H_2O)_6^{2+}$.[8, 9] All structures are fully relaxed until the electronic energy and force acting on the atom were smaller than 10^{-4} eV and 0.02 eV·$Å^{-1}$, respectively. The Brillouin-zone sampling is conducted using Monkhorst-Pack (MP) grids of special points with a separation of 0.04 $Å^{-1}$. The self-consistent field iteration is accelerated by Gaussian smearing of 0.05 eV. A vacuum height of >15 Å along the vertical direction is selected to avoid the unwanted interaction between the slab and its period images. The optimized structures, charge density difference, and ELF plots are illustrated with VESTA software.[10]

The adsorption energy (E_{ads}) of adsorbate A is defined as:

$$E_{ads} = E_{A/surf} - E_{surf} - E_A$$

where $E_{A/surf}$, E_{surf}, and E_A are corresponding to the energy of adsorbate A adsorbed on the surface, the energy of the clean surface, and the energy of isolated A, respectively.

The insertion energy (E_{ins}) of A is defined as:

$$E_{ins} = E_{A/inserted} - E_{A/surf}$$

where $E_{A/inserted}$ is corresponding to the energy of A inserted in the surface.

Figures

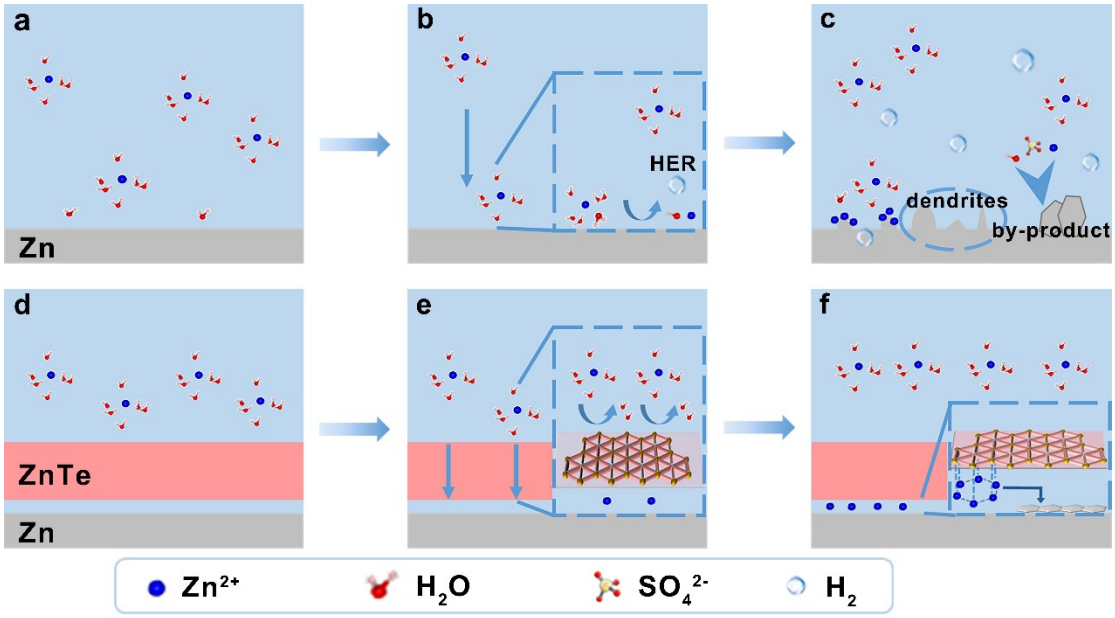

Fig. S1. The initial state, desolvation, and Zn plating process on (a, b, c) bare Zn and (d, e, f) ZnTe@Zn.

As shown in Fig. S1, the surface of different electrodes during the zinc deposition process is different. It is obvious that bare Zn and H_2O can be in direct contact, while the contact between ZnTe@Zn and water is hindered by the ZnTe layer (Fig. S1a and d). The desolvation of $Zn(H_2O)_6^{2+}$ is required before Zn plating. In this process, a hydrogen evolution reaction (HER) will occur on the bare Zn anode with the generation of OH^- (Fig. S1b). Subsequently, as shown in Fig. S1c, the formation of dendrites and the appearance of H_2 will occur on bare Zn anode due to the tip effect and the generation of the by-product. In contrast, with the improved desolvation and induced Zn plating of the ZnTe layer, the flatter deposition and the restricted hydrogen evolution are realized on the ZnTe@Zn anode (Fig S1d and e).

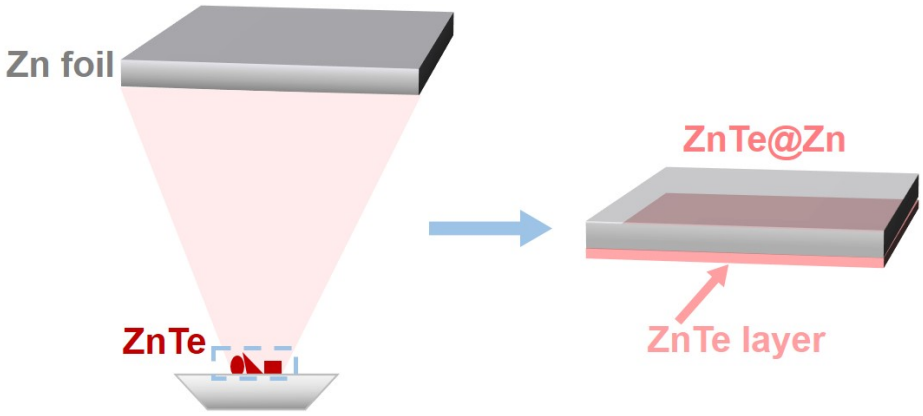

Fig. S2. Schematic illustration of uniform growth of ZnTe layer on Zn foil via thermal evaporation.

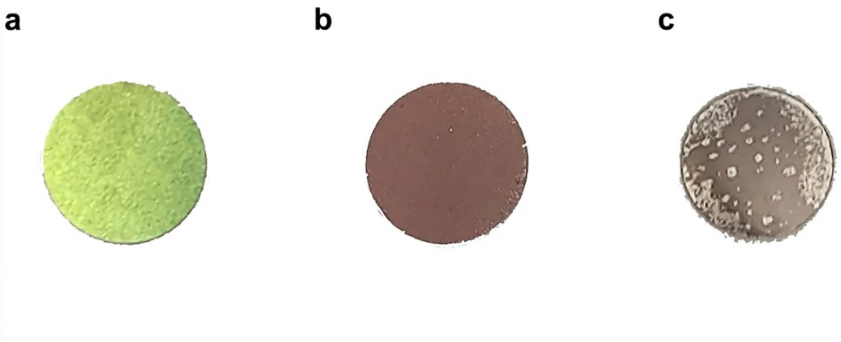

Fig. S3. Photographs of ZnTe@Zn prepared with different target masses: (a) 0.10 g; (b) 0.35 g; (c) 0.60 g.

When the thickness of the ZnTe layer is too thick, the adhesion of ZnTe on the Zn substrate is insufficient, resulting in a relatively rough surface (Fig. S2c; edge detachment occurs during punching).

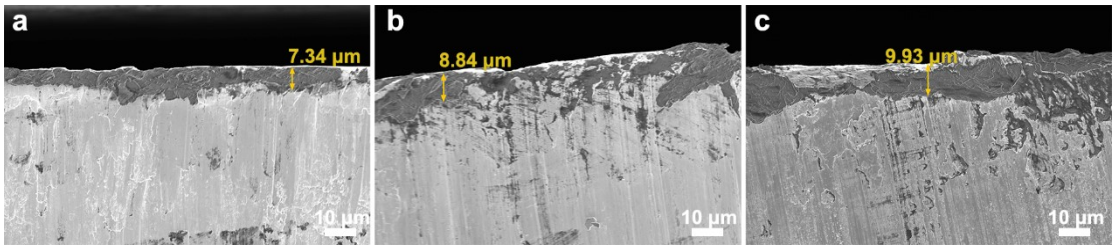

Fig. S4. Side-view SEM images of ZnTe@Zn foil with different thicknesses of ZnTe layer: (a) 7.34 μm; (b) 8.84 μm; (c) 9.93 μm.

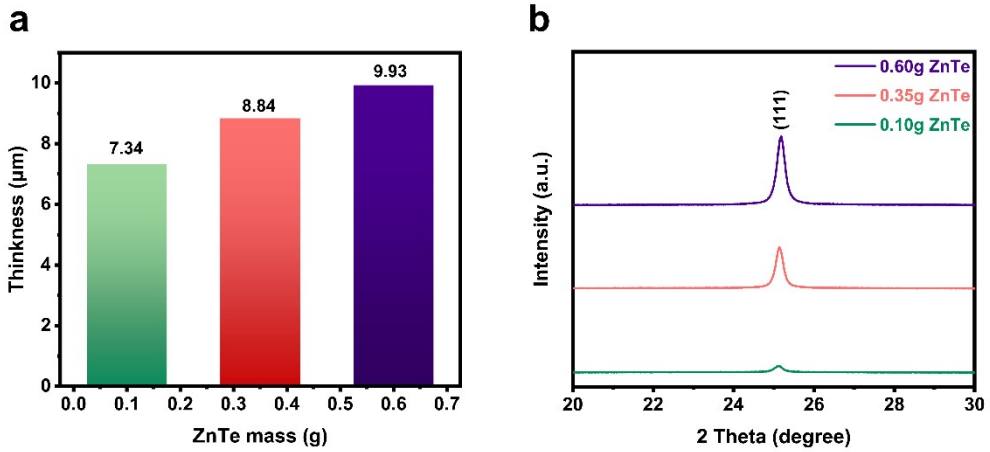

Fig. S5. (a) Thickness histogram of ZnTe layer grown with different target mass. (b) XRD patterns of different ZnTe@Zn anodes.

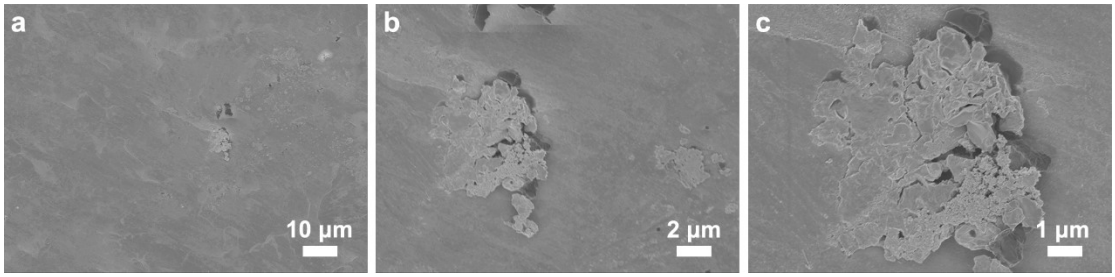

Fig. S6. Top-view SEM images of bare Zn at different magnifications. There are some irregular morphologies on the bare Zn anode.

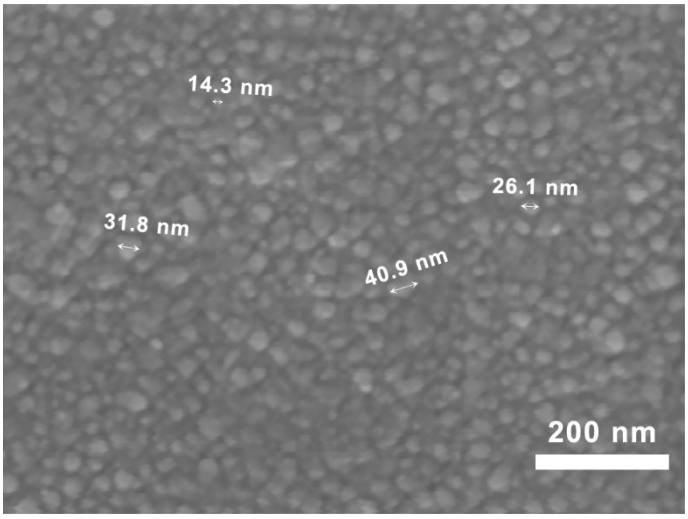

Fig. S7. Top-view SEM images of the ZnTe@Zn ("0.35 g") At larger magnification.
The size of ZnTe (10-40 nm) is obtained by scale conversion and measurement.

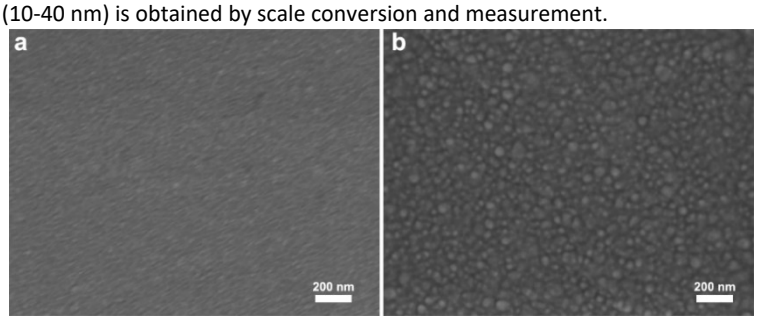

Fig. S8. Top-view SEM images of (a) 7.34 μm thick ZnTe@Zn ("0.10 g"), (b) 9.93 μm thick ZnTe@Zn ("0.60 g").

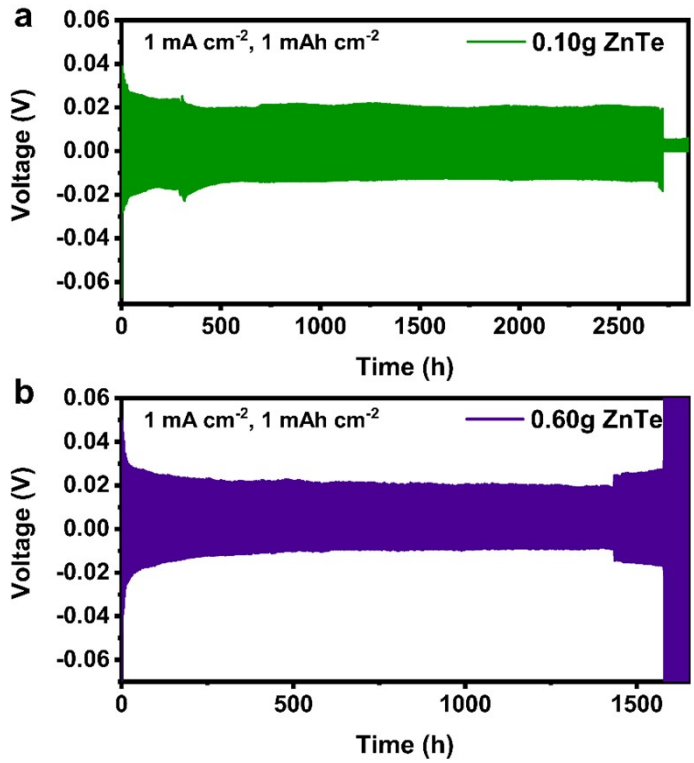

Fig. S9. Long-term galvanostatic cycling of (a) "7 μm" (target weight: 0.10 g) ZnTe@Zn and (b) "10 μm" (target weight: 0.60 g) ZnTe@Zn symmetric cells at 1 mA cm^{-2}, 1 mAh cm^{-2}.

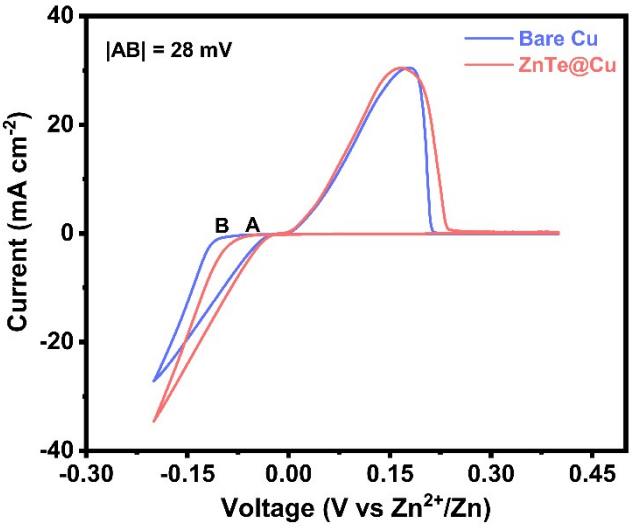

Fig. S10. CV curves of Zn||Cu cells using bare Cu and ZnTe@Cu at 1 mV s^{-1}.

Compared with bare Cu, the more positive onset potential for Zn deposition of ZnTe@Cu confirms the lower nucleation energy barrier. And the higher current during Zn deposition means accelerated reaction dynamics.

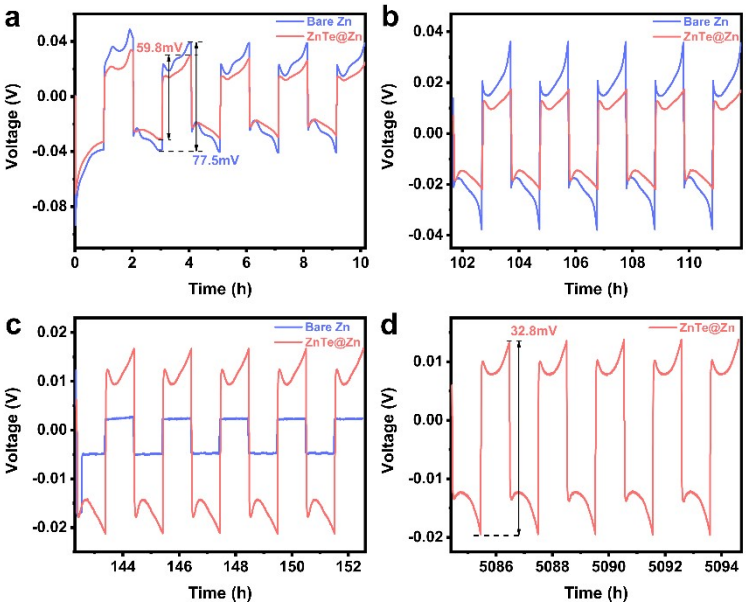

Fig. S11. Enlarged voltage profiles of ZnTe@Zn during different stages at 1 mA cm^{-2} and 1 mAh cm^{-2}. (a) The early stage of the cycle. (b) and (c) the Middle stage of the cycle. (d) The later stage of the cycle.

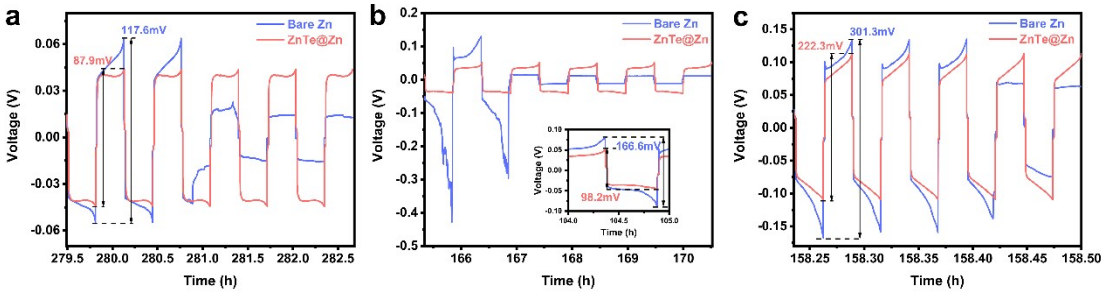

Fig. S12. (a) Enlarged voltage profiles near short circuit of bare Zn at 10 mA cm^{-2} and 3 mAh cm^{-2}. (b) Enlarged voltage profiles near short circuit of bare Zn at 10 mA cm^{-2} and 5 mAh cm^{-2}. The inset shows the hysteresis voltage during the stable cycle. (c) Enlarged voltage profiles near short circuit of bare Zn at 40 mA cm^{-2} and 1 mAh cm^{-2}.

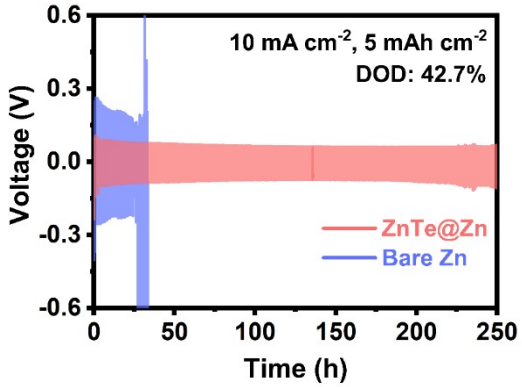

Fig. S13. The high depth of discharge (DOD) tests of bare Zn and ZnTe@Zn symmetric cells at a current of 10.0 mA cm^{-2} and a capacity of 5.0 mAh cm^{-2}. The thickness of the used Zn foil is 20 μm, corresponding to a DOD of about 42.7%.

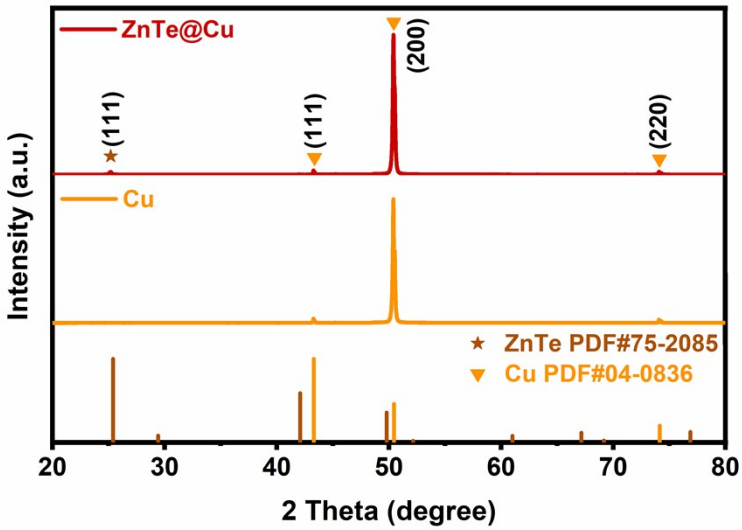

Fig. S14. XRD patterns of bare Cu and ZnTe@Cu electrode. ZnTe@Cu shows a peak around 25 degrees of ZnTe(111), indicating the preferred deposition of ZnTe.

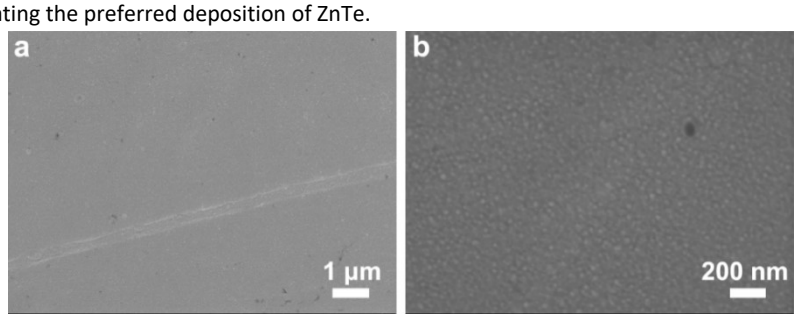

Fig. S15. SEM images of ZnTe@Cu at different magnifications. The topography of ZnTe on Cu foil is the same as that on Zn foil.

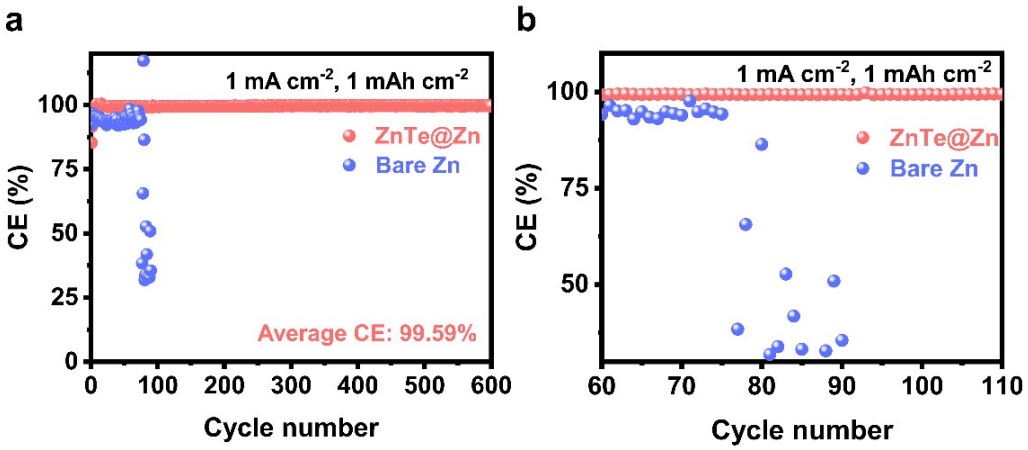

Fig. S16. CE tests of the asymmetrical ZnTe@Cu||Zn and bare Cu||Zn cells at 1 mA cm^{-2} and 1 mAh cm^{-2}. (a) Overview of the CE curve. (b) The CE curve around cell failure.

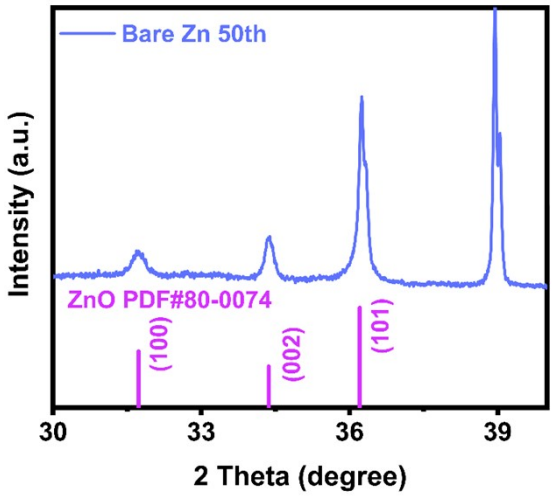

Fig. S17. XRD pattern of bare Zn anode after 50 cycles, and compare it with the standard PDF of ZnO.

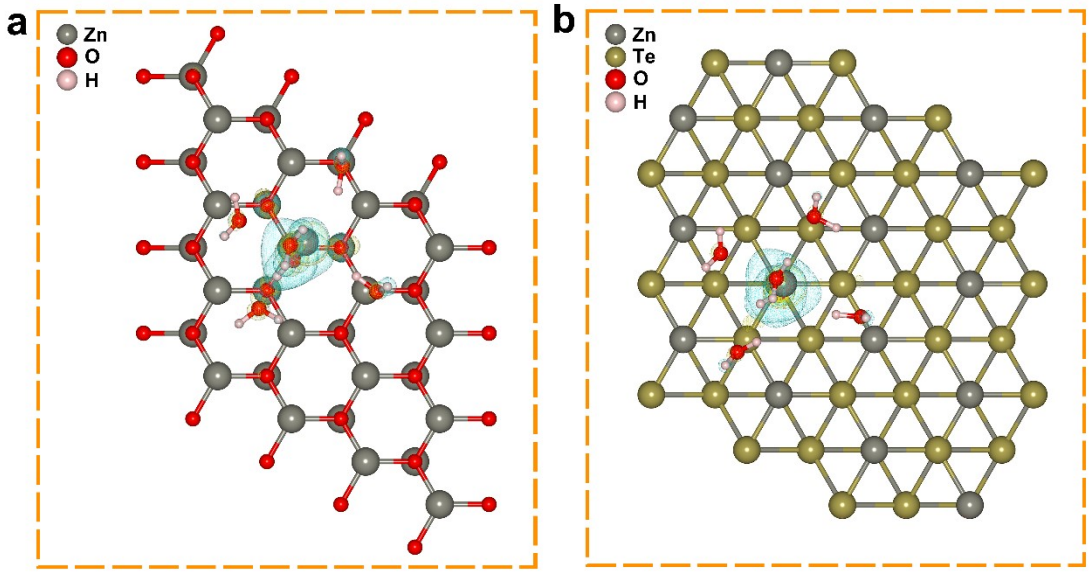

Fig. S18. The top-views of charge differential densities of (a) ZnO and (b) ZnTe with water sheath layer at steady state.

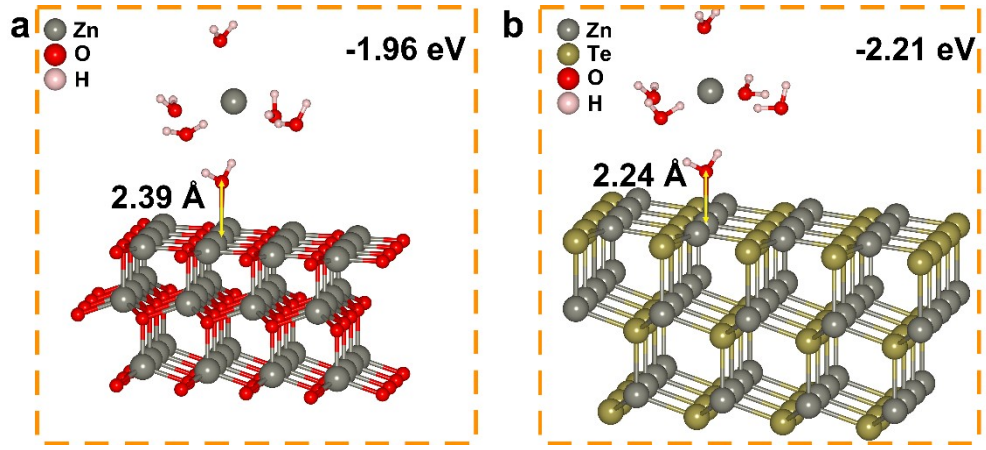

Fig. S19. Schematic diagrams of the bonding between $Zn(H_2O)_6^{2+}$ and (a) ZnO or (b) ZnTe at steady state. The O-Zn bond length of ZnTe is 2.24 Å, which is shorter than that of ZnO (2.39 Å), indicating a stronger interaction.

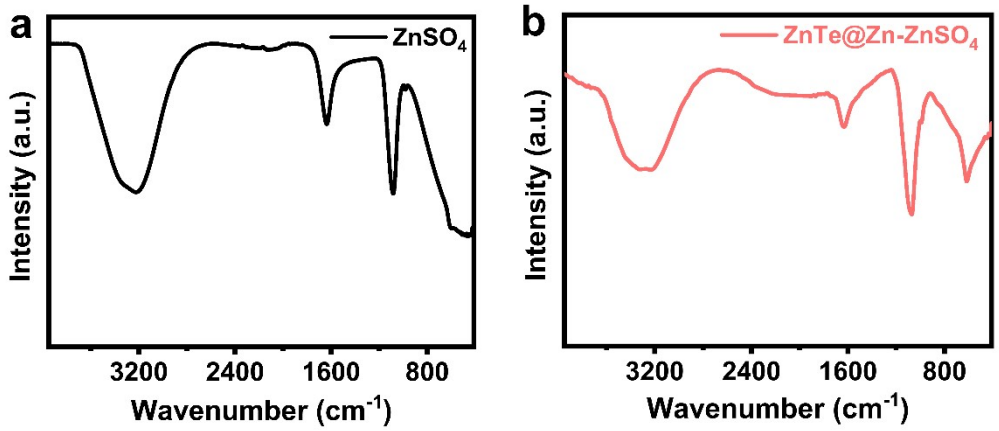

Fig. S20. FT-IR spectra of (a) $ZnSO_4$ and (b) ZnTe@Zn immersed into 2 M $ZnSO_4$ (ZnTe@Zn-$ZnSO_4$) ranging from 400 to 3800 cm^{-1}.

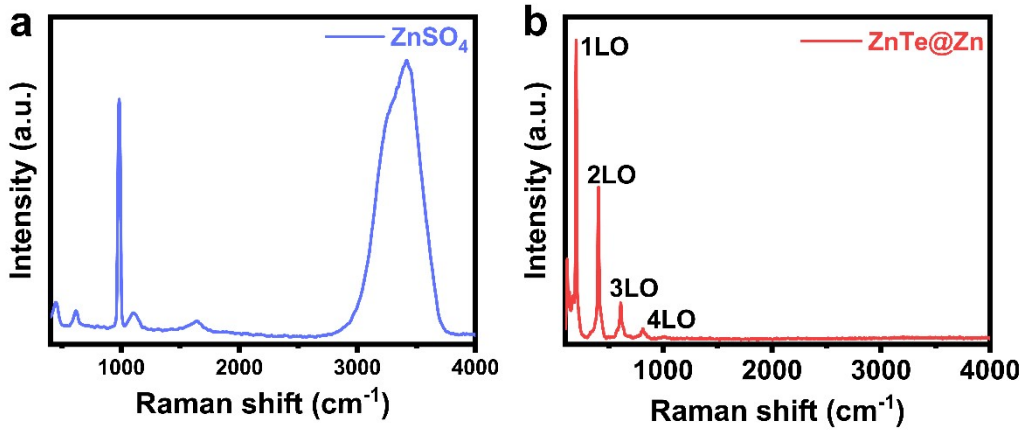

Fig. S21. Raman spectra of (a) 2 M $ZnSO_4$ and (b) ZnTe@Zn.

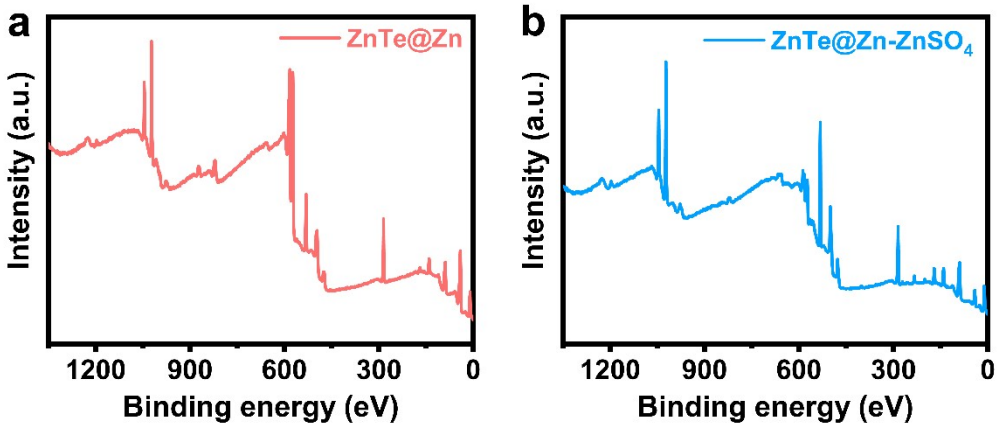

Fig. S22. XPS spectra of ZnTe@Zn (a) before and (b) after being immersed into 2 M $ZnSO_4$.

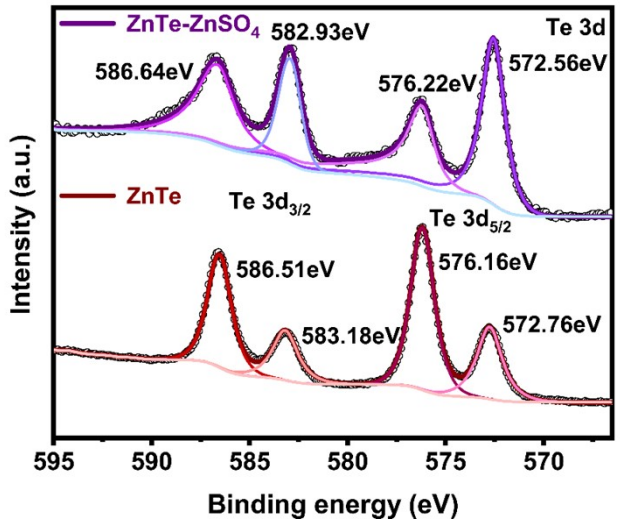

Fig. S23. XPS spectra of Te3d. The ZnTe and ZnTe-$ZnSO_4$ represent ZnTe@Zn before and after being immersed into 2 M $ZnSO_4$. The negative charge of Te increases after participating in the interaction with H_2O, resulting in lower electron binding energy overall.

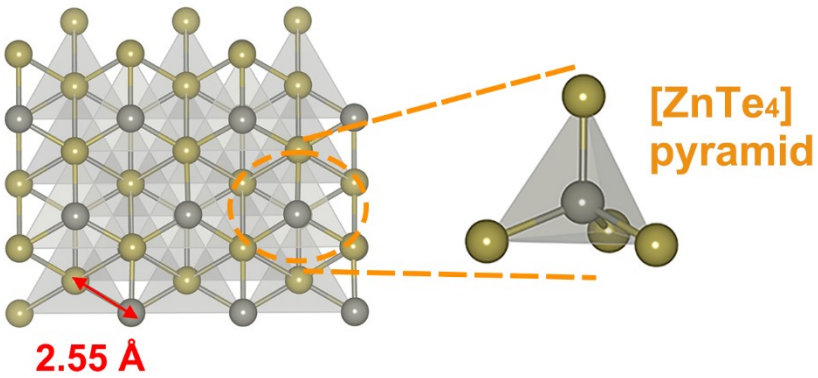

Fig. S24. The crystal structure of ZnTe along the direction of [111]. The Pyramidal [$ZnTe_4$] unit is shown in an enlarged view, providing a tunnel structure with a 2.55 Å edge length along the [111] direction for Zn^{2+} transport.

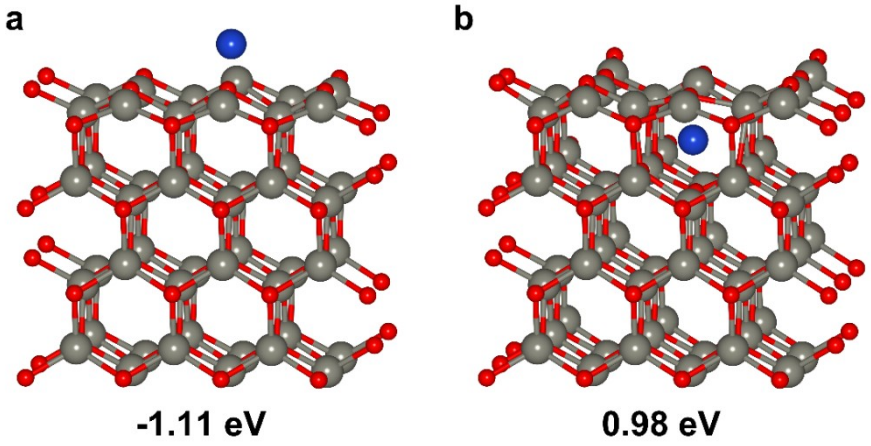

Fig. S25. The side views of adsorbed and inserted Zn^{2+} in ZnO(100). The adsorption energy and insertion energy are calculated with initial-state energy as a reference.

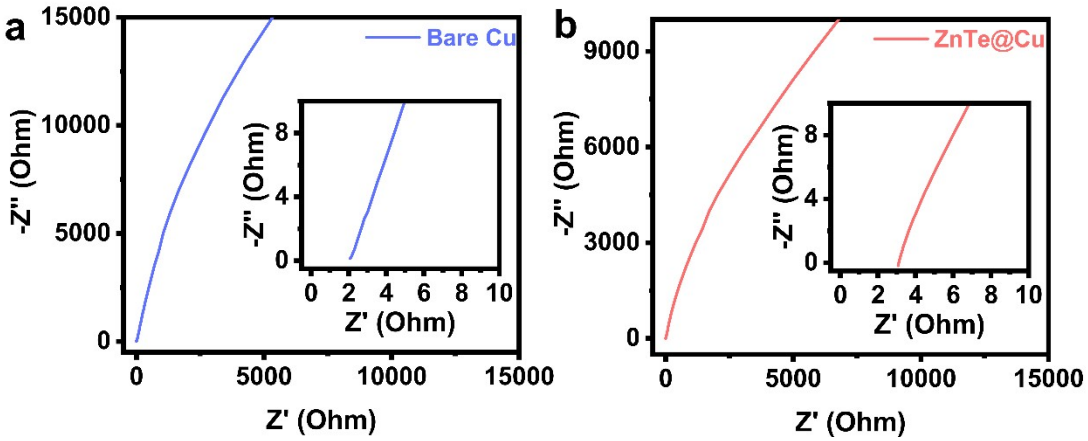

Fig. S26. (a) Nyquist plot of Cu||Cu symmetric cell. (b) Nyquist plot of ZnTe@Cu||ZnTe@Cu symmetric cell. Based on the EIS profiles, the ionic conductivity of the ZnTe layer is obtained. The resistance of ZnTe layer is calculated: R(ZnTe) = R(total) – R(glass fiber) = (3.123 – 2.087) Ω = 1.036 Ω**.** Then the ionic conductivity of the ZnTe layer could be calculated to be about 8.5×10^{-4} S cm^{-1} by the formula: $\sigma = L/(R \times S)$, where L is the thickness of the ZnTe layer (8.84 μm), R is the resistance of the ZnTe layer, and S is the contact area (1 cm^{-2}).

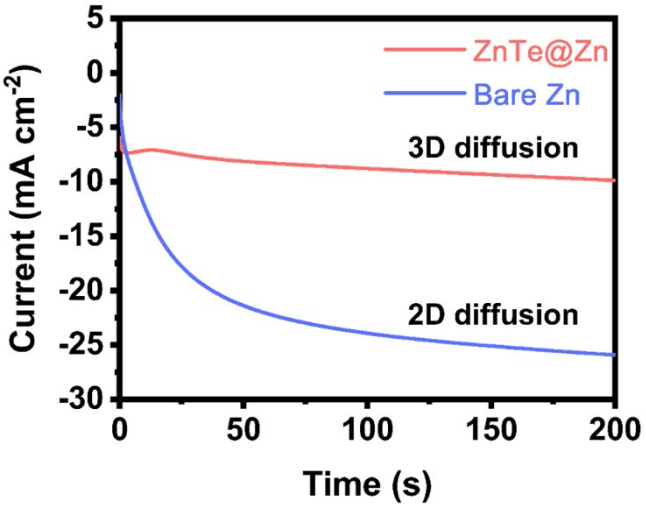

Fig. S27. Chronoamperometry curves of ZnTe@Zn and bare Zn symmetric cells at a constant potential of –150 mV. The change of current with time at constant potential reflects the nucleation process. The Zn deposition is influenced by mass transfer, so it can be assumed that the rise in current is caused by an increase in electrode surface area.

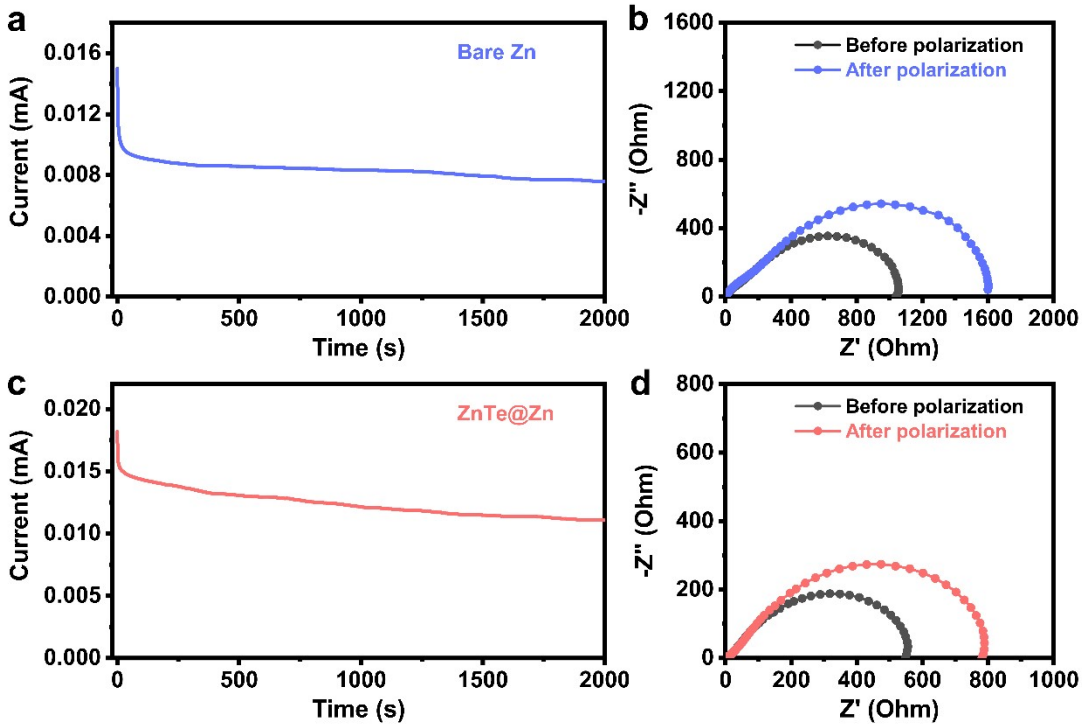

Fig. S28. The Zn-ion transference number measurement. (a) Variation of current with the time of Zn||Zn symmetric cell under polarization of 20 mV for 2000 s. (b) Nyquist plots of Zn||Zn cell before and after polarization. (c) Variation of current with the time of ZnTe@Zn|| ZnTe@Zn symmetric cell under polarization of 20 mV for 2000 s. (d) Nyquist plots of ZnTe@Zn|| ZnTe@Zn cell before and after polarization. The Zn^{2+} transference number ($t_{Zn^{2+}}$) can be calculated by the following equation:

$$t_{Zn^{2+}} = \frac{I_S(\Delta V - I_0 R_0)}{I_0(\Delta V - I_S R_S)}$$

where $\triangle V$ is the constant potential polarization (20 mV), I_0 and R_0 are the initial current density and charge transfer resistance and I_s and R_s are the steady-state current density and charge transfer resistance. The I_0/I_s for bare Zn and ZnTe@Zn cells are 15/7.56 μA and 18/11 μA, respectively; The R_0/R_s for bare Zn and ZnSe@Zn cells are 1040/1600 Ω and 549/782 Ω, respectively. By comparison, the calculated $t_{Zn^{2+}}$ (bare Zn) is 0.28, while the ZnTe@Zn||ZnTe@Zn cell has a larger $t_{Zn^{2+}}$ of 0.54. The results indicate that the ZnTe layer improves the transport of Zn^{2+} to realize the more conduction of effective Zn^{2+} while inhibiting the appearance of by-product $Zn_4SO_4(OH)_6{\cdot}4H_2O$.

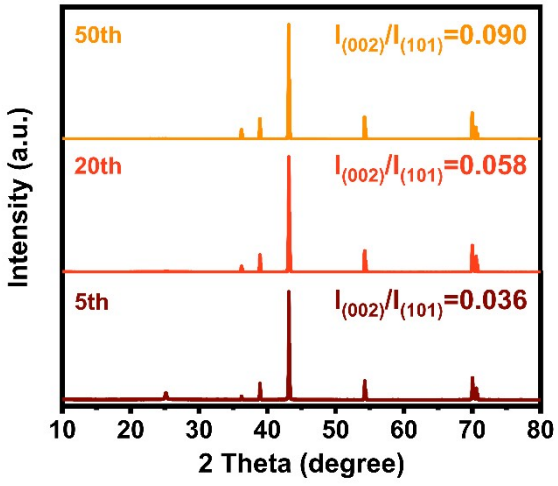

Fig. S29. XRD patterns of ZnTe@Zn anode in Zn||α-MnO_2 full cell after different cycles.

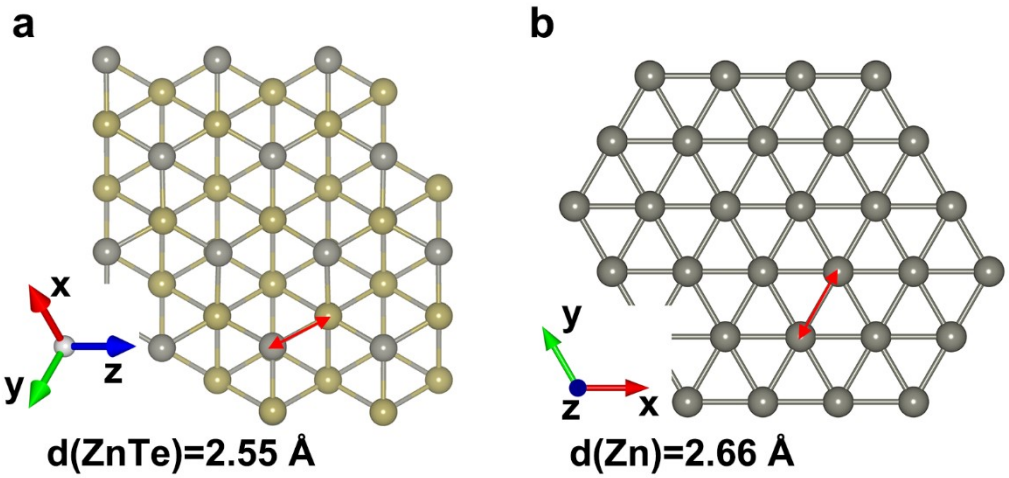

Fig. S30. (a) ZnTe (111) plane and (b) Zn (002) plane. The gray and brown ball represents the Zn and Te atom, respectively. The lattice-matching degree of ZnTe(111) and Zn(002) is 95.8%.

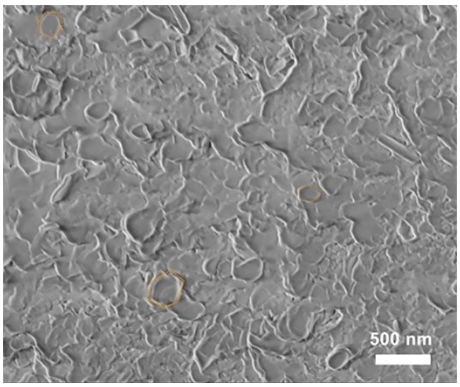

Fig. S31. SEM image of ZnTe@Zn anode after 5 cycles at higher magnification (10k). It is found that there are some small hexagonal structures.

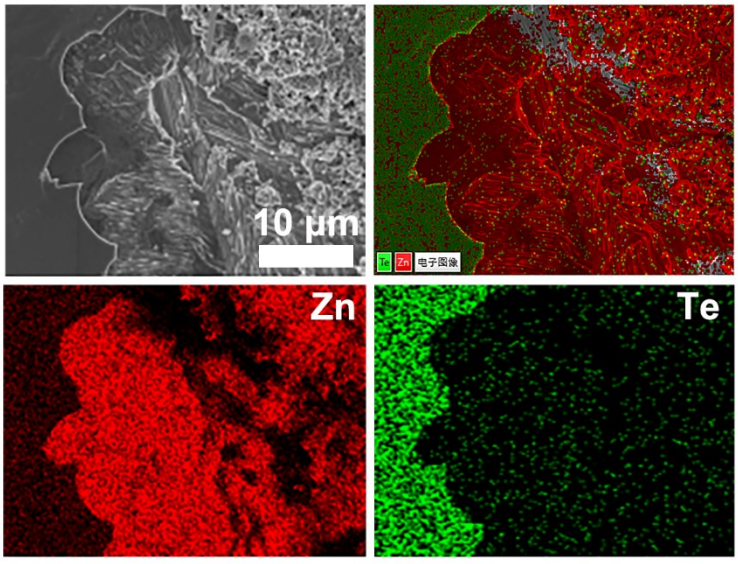

Fig. S32. SEM image and EDX mapping images of deposited Zn on ZnTe@Zn anode. The results show that Zn is deposited beneath the ZnTe layer.

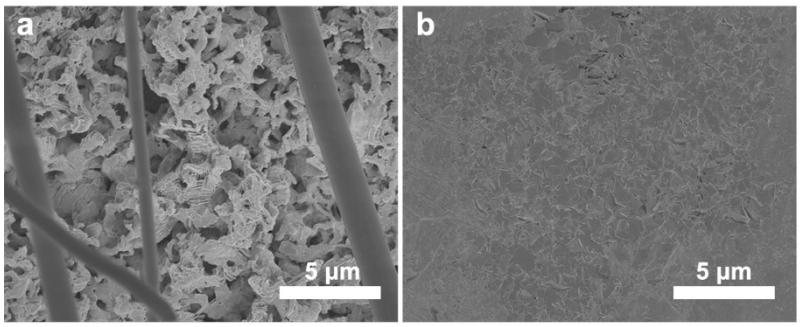

Fig. S33. SEM images of (a) bare Zn and (b) ZnTe@Zn anodes after 50 cycles at 1 mA cm^{-2} and 1 mAh cm^{-2}. The plated Zn on ZnTe@Zn is flatter than bare Zn. Glass fibers and irregular aggregation of Zn appear on the bare Zn.

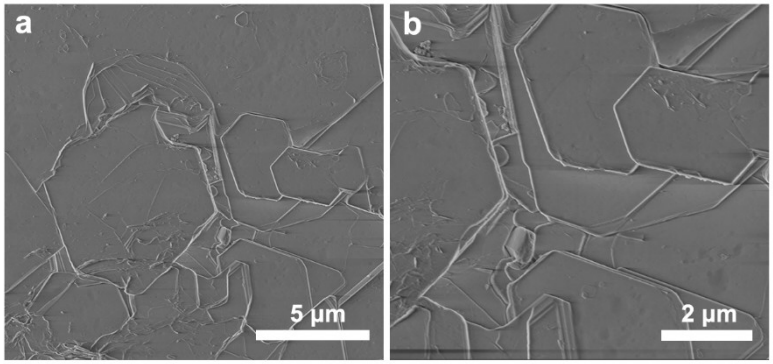

Fig. S34. SEM images of ZnTe@Zn anode after running 2000 h at different magnifications. It is clear that hexagonal Zn deposited on the surface of ZnTe@Zn.

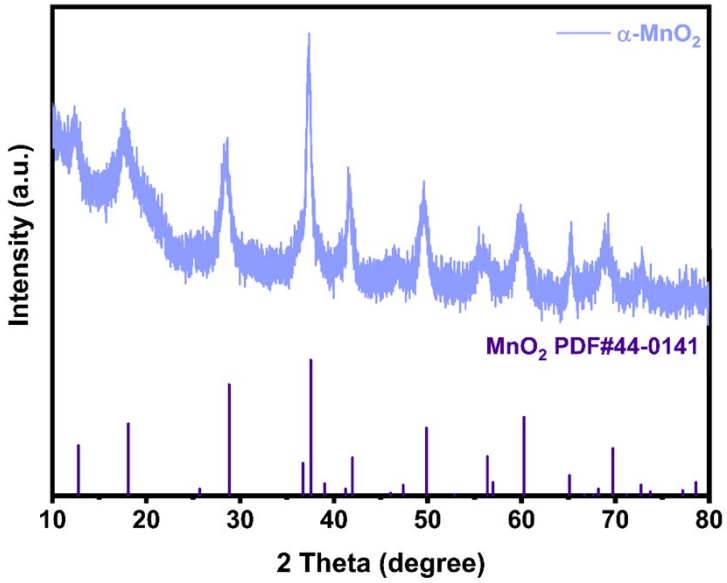

Fig. S35. XRD pattern of α-MnO_2 cathode material.

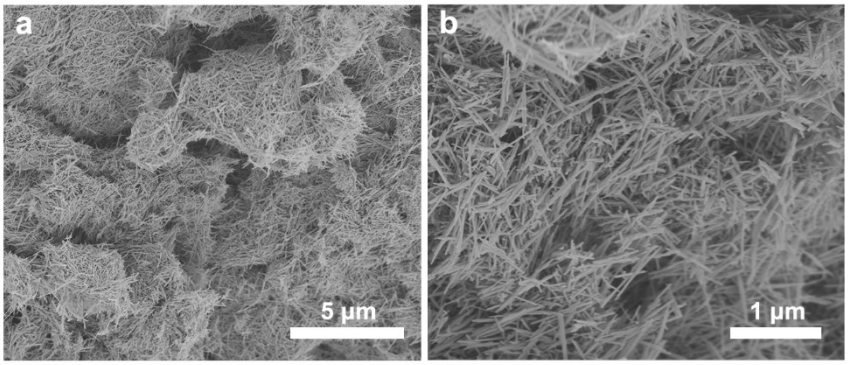

Fig. S36. SEM images of α-MnO_2 cathode material at different magnifications.

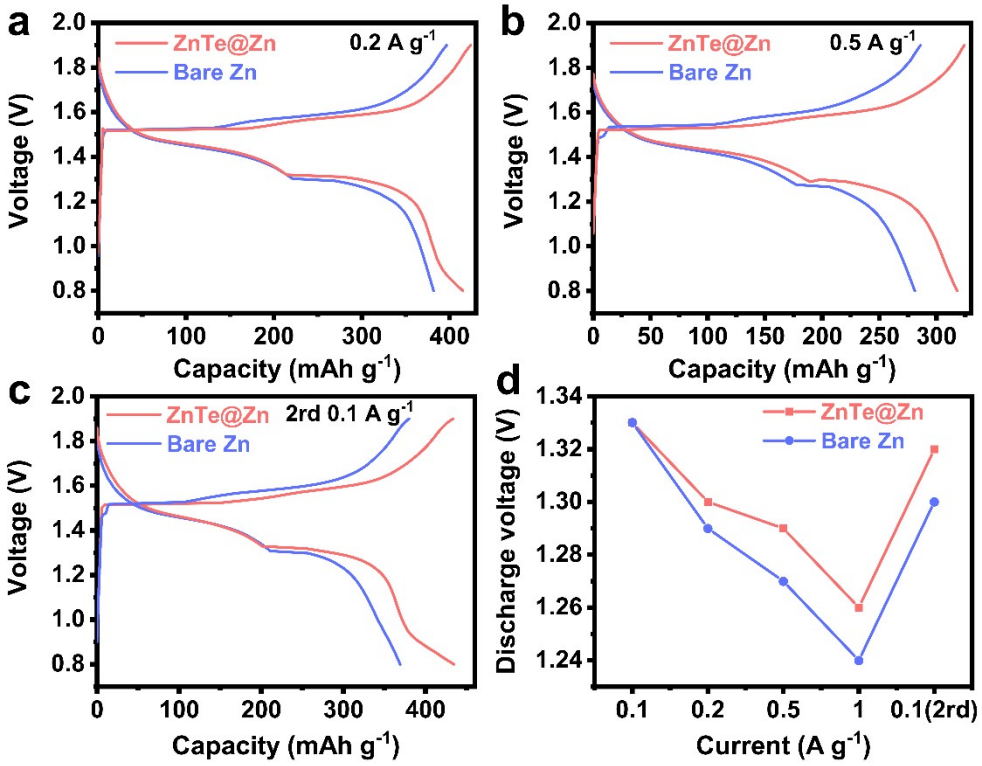

Fig. S37. The charge-discharge curves of full cells using bare Zn and ZnTe@Zn anodes at (a) 0.2 A g^{-1}, (b) 0.5 A g^{-1}, and (c) the second 0.1 A g^{-1}. (d) Comparison of discharge voltage of bare Zn||α-MnO_2 and ZnTe@Zn||α-MnO_2 at different current. The ZnTe@Zn anode provides a higher discharge voltage than the bare Zn anode.

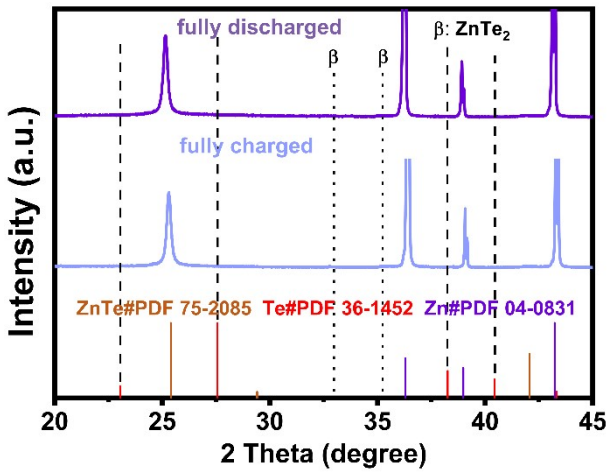

Fig. S38. The enlarged image of XRD diffraction patterns of ZnTe@Zn anodes after full charging/discharging.

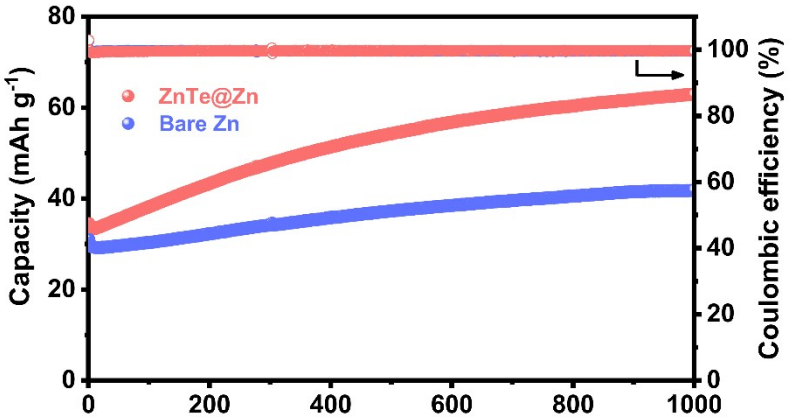

Fig. S39. Long-term cycling performances and CE curves of full cells with AC cathodes at 1 A g^{-1} (based on the AC mass). The AC loading: 1.3 mg cm^{-2}.

References

1 G. Kresse and J. Furthmüller, *Efficiency of ab-initio total energy calculations for metals and semiconductors using a plane-wave basis set*, *Computational Materials Science*, 1996, **6**, 15-50.

2 G. Kresse and J. Furthmüller, *Efficient iterative schemes for ab initio total-energy calculations using a plane-wave basis set*, *Physical Review B*, 1996, **54**, 11169-11186.

3 G. Kresse and J. Hafner, *Ab initio molecular dynamics for liquid metals*, *Physical Review B*, 1993, **47**, 558-561.

4 J. P. Perdew, K. Burke, and M. Ernzerhof, *Generalized Gradient Approximation Made Simple*, *Physical Review Letters*, 1996, **77**, 3865-3868.

5 J. P. Perdew and Y. Wang, *Accurate and simple analytic representation of the electron-gas correlation energy*, *Physical Review B*, 1992, **45**, 13244-13249.

6 G. Kresse and D. Joubert, *From ultrasoft pseudopotentials to the projector augmented-wave method*, *Physical Review B*, 1999, **59**, 1758-1775.

7 P. E. Blöchl, *Projector augmented-wave method*, *Physical Review B*, 1994, **50**, 17953-17979.

8 K. Mathew, V. S. C. Kolluru, S. Mula, S. N. Steinmann, and R. G. Hennig, *Implicit self-consistent electrolyte model in plane-wave density-functional theory*, *The Journal of Chemical Physics*, 2019, **151**, 234101.

9 K. Mathew, R. Sundararaman, K. Letchworth-Weaver, T. A. Arias, and R. G. Hennig, *Implicit solvation model for density-functional study of nanocrystal surfaces and reaction pathways*, *The Journal of Chemical Physics*, 2014, **140**, 084106.

10 K. Momma and F. Izumi, *VESTA 3for three-dimensional visualization of crystal, volumetric and morphology data*, *Journal of Applied Crystallography*, 2011, **44**, 1272-1276.